Article

Grain Boundary Engineering and Its Effect on Intergranular Corrosion Resistance of a Ni-Cr-Mo Based C276 Superalloy

Chi Zhang [1,*], **Ling Lin** [1], **Renchao Chen** [1], **Liwen Zhang** [1] **and Zhiwen Shao** [2]

1   School of Materials Science and Engineering, Dalian University of Technology, Dalian 116024, China
2   Ningbo Branch, Ordnance Science Institute of China, Ningbo 315103, China
*   Correspondence: zhangchi@dlut.edu.cn

Abstract: A Ni-Cr-Mo-based C276 superalloy was cold rolled to 5–40% and annealed at 1050 °C for 30 min. The microstructure and grain boundary character distribution after cold rolling and annealing were characterized. Grain refinement and a certain amount of coincident-site lattice (CSL) boundaries were obtained through recrystallization. The fraction of CSL boundaries reached peak at the cold rolling of 15% and annealing at 1050 °C for 30 min, which was the critical condition for completed recrystallization. In addition, sensitization treatments and double-loop electrochemical potentiokinetic reaction (DL-EPR) tests were applied to the cold rolled and annealed samples. The samples with a high fraction of CSL boundaries showed higher intergranular corrosion resistance as compared to the ones with a low fraction of CSL boundaries. It implies that the intergranular corrosion resistance of C276 superalloy can be enhanced by optimizing the grain boundary structure through cold rolling and annealing.

Keywords: superalloy; cold rolling and annealing; grain boundary engineering (GBE); sensitization; intergranular corrosion resistance

1. Introduction

C276 superalloy is a commonly used material for nuclear energy applications because it has high resistance to corrosion, creep and fatigue at elevated temperatures [1–3]. The long-time service safety requirements of the nuclear energy industry demand that the materials used preserve high performance through alloy design and microstructure optimization. The grain boundary character distribution (GBCD) is found to be related to the resistances of intergranular corrosion (IGC) and stress corrosion cracking (SCC), weldability, low- and high-cycle fatigue, high temperature creep and electrical conductivity, et al. [4–6]. Therefore, one effective way to improve the properties of superalloys is optimizing the GBCD.

The concept of optimizing the material's properties by altering GBCD was initially developed by Watanabe in the early 1980s, which has since been referred as grain boundary engineering (GBE) [7]. The GBE are successfully applied to the materials with low or medium stacking fault energy (SFE), including Ni-based superalloys [8,9], austenite stainless steel [10–12], aluminum [13], et al. The corrosion rate of Alloy 600, a Ni-based superalloy used for nuclear steam generator tubing, decreased dramatically by increasing the percentage of the coincident site lattice (CSL) boundary through GBE processing [5]. The susceptibility to intergranular oxidation was also reduced in IN718 superalloy with a high fraction of low-Σ value CSLs [14]. Additionally, Chen et al. pointed out the chromium depletion was inhibited by the twin boundaries, remarkably promoting the IGC resistance [15].

Much research has been devoted to investigating the GBE methods, in which the prime aim is usually to promote the fraction of CSLs. The values of coinciding sites for the neighboring lattices of CSLs are denoted as Σ. Among the CSLs, Σ3 grain boundaries show pronounced fractions and are relevant to the material properties. Randle investigated

the twining-related grain boundary development during recrystallization and proposed a model to describe the generation of Σ3 grain boundaries associated with twins [16,17]. For the Σ3 boundaries, the coherent twin (having {111} grain boundary plane) and incoherent twin (having {112} or other grain boundary planes) were defined and found to have different contributions to the material properties [5,18]. The GBCD can be manipulated through thermo-mechanical processing (TMP). A certain degree of deformation followed by high temperature short-time annealing shows pounced effects on promoting the percentage of low-Σ value CSL [19]. Sahu et al. achieved a high fraction (77% length fraction) of low-Σ CSLs in Alloy 600 using hot rolling and short-time annealing treatment [20]. Cao et al. investigated the microstructure evolution of Incoloy 800H superalloy during hot rolling and solution treatment, especially focused on the GBCD [21,22]. Akhiani et al. studied the macro-texture and micro-texture evolution in Incoloy 800H/HT superalloy via continuous cold rolling and cross cold rolling and annealing [23,24]. Their works indicate that the evolution of $\Sigma 3^n$ type boundaries relates with the cold rolling paths and strains. Jones et al. found that the promotion of Σ3 and Σ9 boundaries through GBE can reduce the sensitization and IGC tendency greatly for 304 austenite stainless steel [25].

However, limited works about the variations in GBCD for C276 superalloy during cold rolling and annealing are available. In this work, the GBCD of C276 superalloy after cold rolling and annealing was characterized and quantified. A sensitization test was also applied to the processed C276 superalloy to evaluate the relation between GBCD and IGC resistance.

2. Experimental Procedure

2.1. Processing and GBCD Detection

The as-received material is a commercial C276 bar with the diameter of 20 mm in a solid solution state. The chemical composition of the bar is listed in Table 1. Figure 1 schematically shows the experiment procedure. Rectangular samples with $70 \times 18 \times 5 \ \text{mm}^3$ were machined from the bar. The samples were subjected to cold rolling with lubricant using a laboratory rolling machine. The total cold rolling reductions were 5%, 10%, 15%, 20%, 30% and 40%. The rolling direction was kept the same for all the passes to model the continuous cold rolling process. The cold rolled samples were then annealed at 1050 °C for 30 min followed by water quenching to acquire an equiaxed grain structure.

Table 1. Chemical composition of the as-received C276 superalloy (wt.%).

C	Si	Mn	S	Cr	Mo	Fe	W	Co	Cu	Ni
0.004	0.01	0.40	<0.002	16.00	16.34	5.98	3.46	0.25	0.04	Bal.
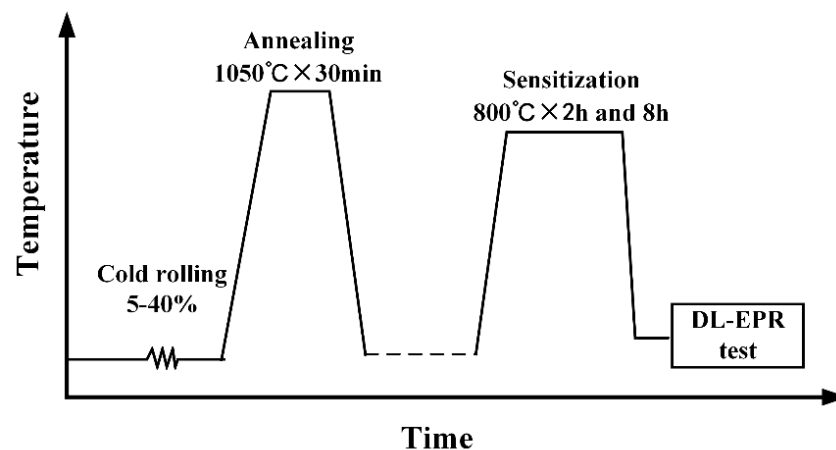
Figure 1. Schematic illustration of the processing, sensitization and IGC test.

To characterize the GBCD, an EBSD detector, which was equipped in a field emission SEM (Zeiss Supra 55), was applied with the accelerating voltage of 20 kV. Before detection, the specimens were electrochemical polished in a solution of 80% CH_3OH and 20% H_2SO_4 at 25 V for 25–30 s. The regions at 1/4 thickness of the transverse plane (RD-TD) were examined. The data were typically obtained with a step size of 0.6–0.8 μm, and over 90% of the tested data were indexed. Then, the data were processed using OIM analysis 5.3 software. The single iteration method with a grain tolerance angle of 5° and minimum grain size of 2 μm was performed to filter the mis-indexing and non-indexing data. The Brandon criterion was used to define the mis-orientation relations of CSL boundaries.

### 2.2. Sensitization Treatment and IGC Test

The tested that C276 superalloy possesses excellent corrosion resistance due to the high alloy design. To evaluate the corrosion resistance of the samples, a sensitization treatment was applied first, as also shown in Figure 1. The cold rolled and annealed samples were heated at 800 °C for 2 h or 8 h followed by water quenching to accelerate the sensitization, in which the sensitized temperature is higher than the maximum service temperature of 650 °C.

Specimens in 15×15 mm^2 were machined from the sensitization treated samples and mechanically polished to assure the surface roughness of $Ra \leq 0.25$ μm. The samples were then ultrasonically cleaned in acetone and kept in a vacuum desiccator before tests. A double-loop electrochemical potentiokinetic reaction (DL-EPR) test was performed to determine the IGC resistance. The electrolyte of a 4 mol/L HCl solution at a temperature of 50 °C was used, as it had already been optimized in a previous paper [26]. A saturated calomel electrode (SCE) is used as the reference electrode. The scan was started from the potential of -0.3 VSCE to the potential of 0.6 VSCE and then reversed to the beginning. The peak current densities in the anodic scan loop (I_a) and reverse scan loop (I_r) were determined from the DL-EPR curves. Then, the ratio of I_r/I_a was defined as the degree of sensitization according to the GB/T 29088–2012. All tests were performed in triplicate to validate the obtained results.

3. Results

### 3.1. GBCD of the As-Received Material

Figure 2 shows the microstructure, microtexture and grain boundary structure of the as-received C276 superalloy bar in a solid solution state. After solution treatment, uniform equiaxed grains with an average diameter of 42 μm were obtained. The inverse pole figure (IPF) map, which is colored by a stereographic triangle corresponding to crystallographic direction, depicts a very weak texture. Based on the quantitative data of crystal orientations obtained, the nature of the grain boundary and misorientation between adjacent grains can be calculated, as shown in Figure 2b. The low angle grain boundary (LAGB) is defined by a misorientation between adjacent grains $\theta < 15°$, while HAGB is defined by $\theta \geq 15°$. The main CSL boundaries, Σ3, Σ9 and Σ27, were also highlighted. Figure 2b depicts that the boundaries are mainly HAGBs with a few LAGBs and a certain number of CSL boundaries formed, in which the fraction of the Σ3 boundary is much higher than others. Some Σ3 boundaries are observed to terminate at the grain interiors.
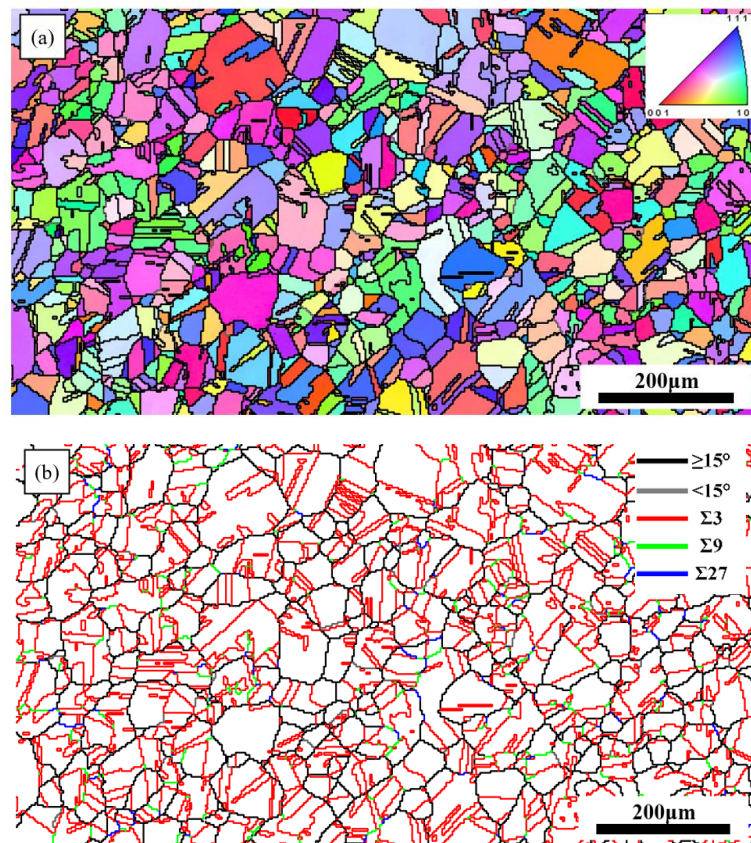
Figure 2. IPF map (**a**) and GBCD map (**b**) of the initial microstructure for the tested C276 superalloy.

3.2. Variations of GBCD after Cold Rolling and Annealing

Figure 3 shows the IPF maps of the tested C276 superalloy after cold rolling and annealing. The microstructures mainly compose an equiaxed grain structure with a certain amount of twins in the grain interiors. Some bands along the rolling direction with small grains can be observed.
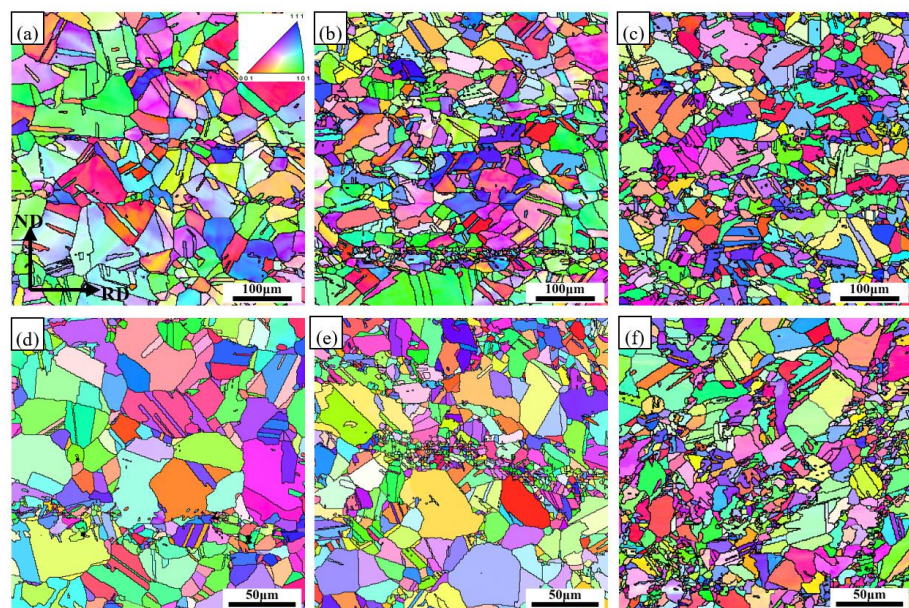
Figure 3. IPF maps of C276 superalloy annealed at 1050 °C for 30 min with different cold rolling reductions. (**a**) 5%, (**b**) 10%, (**c**) 15%, (**d**) 20%, (**e**) 30%, (**f**) 40%.

Grain orientation spread (GOS) maps were also presented based on the EBSD data, as shown in Figure 4. The GOS values decreased dramatically with the increasing cold rolling reduction. The annealed sample with a 5% reduction has grains with GOS around 1~4°. With the rolling reduction increases to 10%, the GOS values of about half part of the grains transfer to less than 1°. The grains have a GOS within almost 1° after cold rolling over 15%. The GOS characters relate the microstructure evolution during annealing. Recovery and grain growth are supposed to occur for the sample with a 5% cold rolling reduction during the annealing process, causing the grains to still have relative higher GOS values. Partial recrystallization occurred for the sample with a 10% cold rolling reduction during annealing. When the cold rolling reduction increases to higher than 15%, almost complete recrystallization with the formation of new dislocation free recrystallized grains occurred, thus causing the GOS of grains to be low.
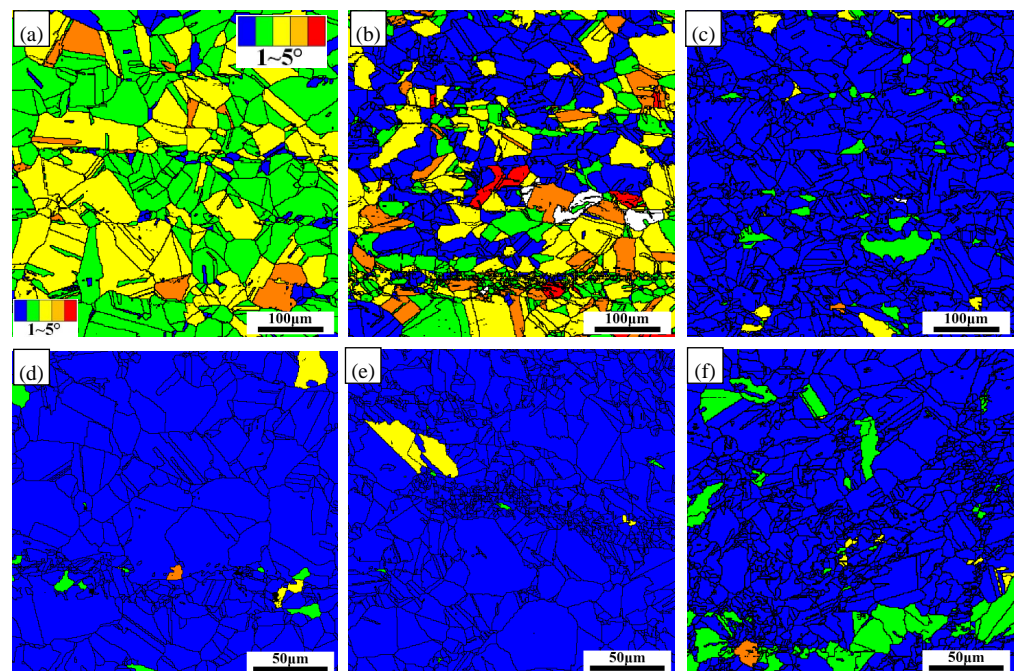

Figure 4. GOS colored maps of C276 superalloy annealed at 1050 °C for 30 min with different cold rolling reductions. (**a**) 5%, (**b**) 10%, (**c**) 15%, (**d**) 20%, (**e**) 30%, (**f**) 40%.

The GBCD can be determined by the local crystallograhpic information of EBSD, as shown in Figure 5. A large fraction of CSL boundaries was formed in the tested C276 superalloy after recovery and recrystallization. In the samples with cold rolling reductions of 5% and 10%, a few of the LAGBs with a gray color can be found.

To elaborate on the variations in the grain boundary character of C276 superalloy during cold rolling and annealing, the GBCD ratio of $\Sigma3/\Sigma9 + \Sigma27$ and grain size were summarized in Figure 6. The status of the initial sample before cold rolling was also shown as a reference. Comparing to the initial sample, the fraction of CSL boundaries decreased linearly after the cold rolling of 5% and 10%. Then, the faction of CSL increased to the maximum value of 67% at a reduction of 15%, which is almost equal to the initial sample. After that, the fraction decreased again until the reduction of 40% with the value of 50%. The ratio of $\Sigma3/\Sigma9 + \Sigma27$ increased first after the cold rolling of 5% and then decreased until the 15% reduction and increased again after that. The grain size of the sample with reduction of 5% was a little higher than the initial one. Then, with the increasing cold rolling reduction, the average grain size decreased.
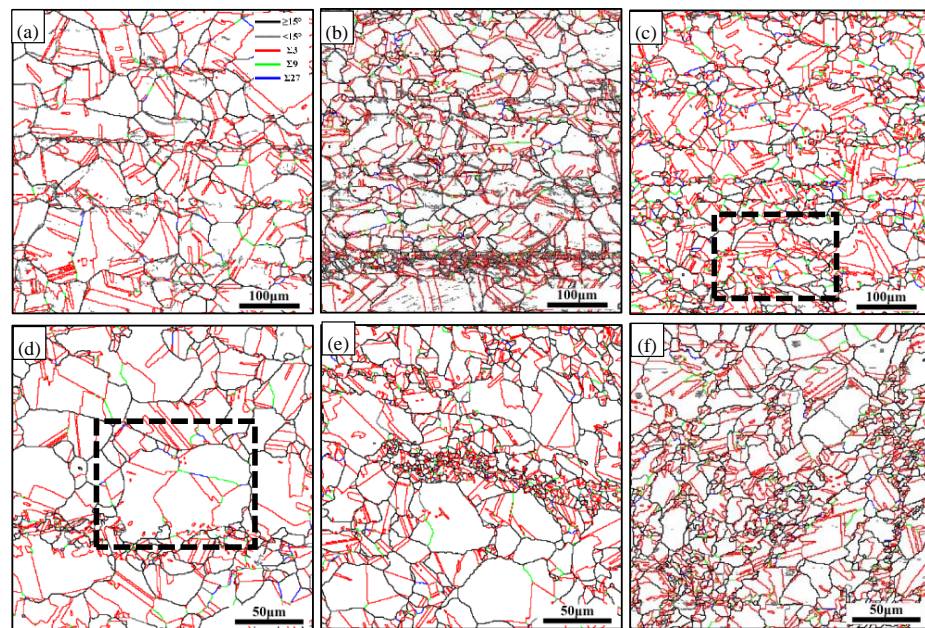
Figure 5. GBCD maps of C276 superalloy annealed at 1050 °C for 30 min with different cold rolling reductions. (**a**) 5%, (**b**) 10%, (**c**) 15%, (**d**) 20%, (**e**) 30%, (**f**) 40%.
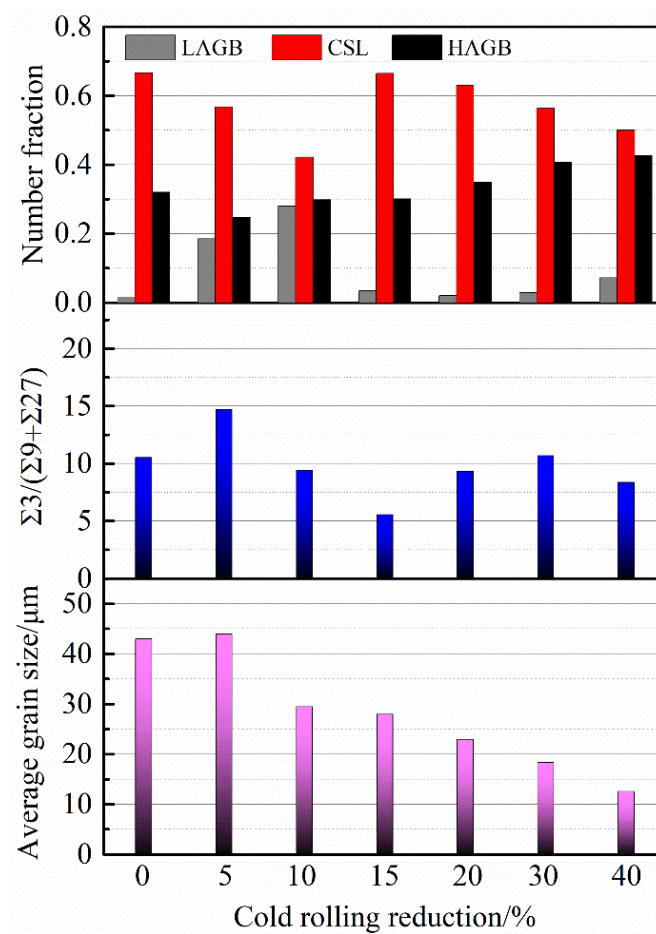
Figure 6. Cold rolling reduction dependent of GBCD, ratio of $\Sigma3/\Sigma9 + \Sigma27$ and grain size of C276 superalloy after annealing at 1050 °C for 30 min. ("0" denotes the initial sample without cold rolling and annealing.)

3.3. Sensitization and IGC Resistance of the Samples with Different GBCDs

The annealed samples with 15% and 40% cold rolling reductions were subjected to the sensitization treatment, in which one had the maximum CSL fraction of 67% and another had a relatively small amount of CSL with the value of 50%. Figure 7 shows the backscatter images of the sensitized samples. It can be seen that precipitates formed and were mainly distributed along grain boundaries after sensitization treatment. There were hardly precipitates in the twin boundary regions. The sensitization time had a vital effect on the precipitation behavior, in which the amounts of precipitates increased as the holding time increased from 2 h to 8 h. The grain boundary length was higher in the sample with a 40% cold reduction as compared to the one with a 15% cold reduction because of the recrystallization. The grain boundaries were observed to serve as the sites for precipitation, resulting in more precipitates formed in the sample with a higher number of grain boundaries.
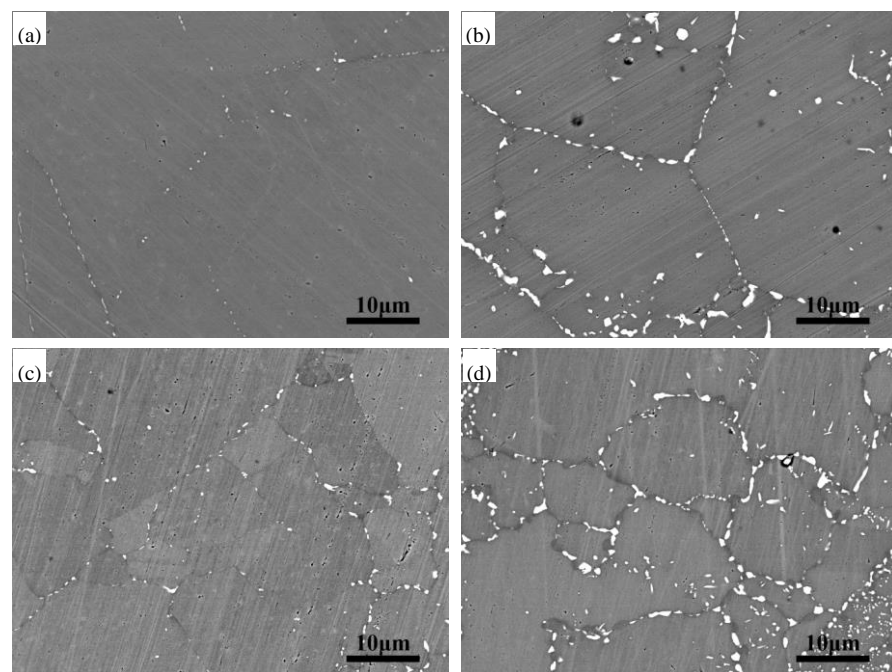
Figure 7. The backscatter images of the sensitized samples with 15% (**a**,**b**) and 40% (**c**,**d**) cold rolling reductions. (**a**,**c**) sensitization at 800 °C for 2 h; (**b**,**d**) sensitization at 800 °C for 8 h.

The DL-EPR curves for the sensitized samples are plotted in Figure 8, showing a typical IGC behavior morphology. In the anodic scan, the curves transferred from the activation zone to the passivation zone, resulting in a peak current (I_a). During the reverse scan, the passivation film was destroyed in the form of an IGC attack, forming another peak current (I_r). The degree of sensitization (I_r/I_a) can be determined from the curves, as noted in the figures. With the increasing sensitization time from 2 h to 8 h, the degrees of sensitization of the sample with a 15% cold rolling reduction increased from 0.60 to 0.74. Furthermore, the degrees of sensitization increased from 0.84 to 0.96 for the sensitized sample with a 40% cold rolling reduction with a sensitization time of 2 h and 8 h, respectively. It can be seen that the sample with a 15% cold rolling reduction had a relatively lower I_r/I_a as compared to the sample with a 40% cold rolling reduction. This implies that the sample with a higher fraction of CSL boundaries and bigger grain size has a better sensitization resistance. It should be mentioned that the ratio of the charge consumed during the reactivation scanning stage to the charge created during the activation scanning stage (Q_r/Q_a) can also be used to estimate the sensitization [27]. However, the anodic scan curves and the reverse scan curves overlapped, making it a little difficult to define the Q_r and Q_a values. Thus, the I_r/I_a values were used in this work [28–30].
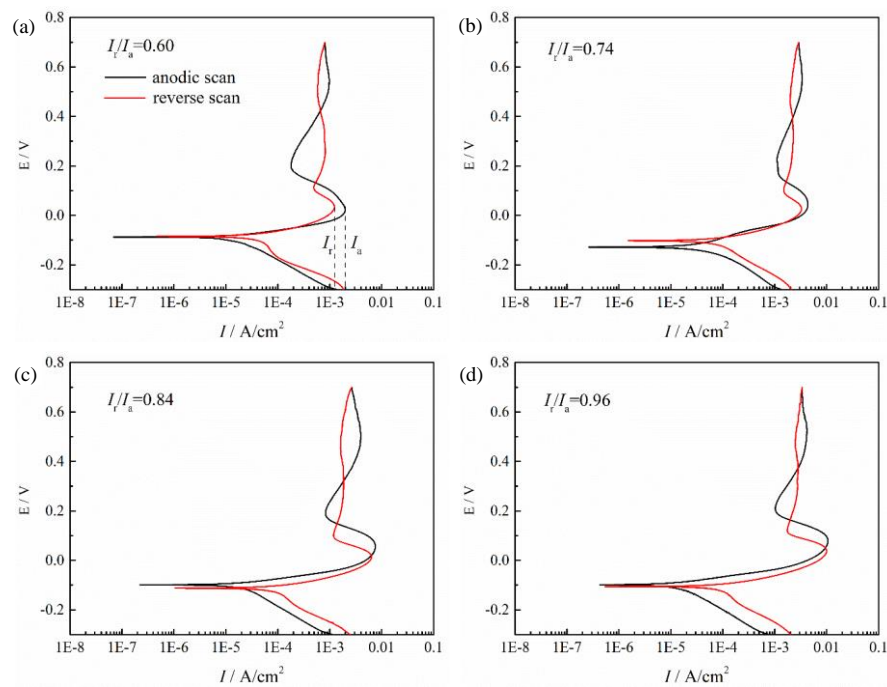
Figure 8. DL-EPR curves of the sensitized samples with 15% (**a**,**b**) and 40% (**c**,**d**) cold rolling reductions. (**a**,**c**) sensitization at 800 °C for 2 h; (**b**,**d**) sensitization at 800 °C for 8 h.

4. Discussion

4.1. Effect of Cold Rolling and Annealing on GBCD

The initial solution-treated C276 superalloy had a high fraction of CSL boundary, as much as 67%. However, the experiment results indicate that these special boundaries cannot stimulate the high density of the twin boundary after cold rolling and annealing. The final annealed samples showed different GBCD conditions varying with cold rolling reduction, as shown in Figure 6. In case of the reduction of 5%, the CSL fraction decreased as compared to the initial one. Static recovery is assumed to be the prime mechanism during annealing, since the grain interior still preserved high orientation deviations, as shown in Figure 4a. The GOS colored map of the 10% cold rolled sample after annealing at 1050 °C for 30 min indicates that about half the population of the grains had GOS values less than 1° (Figure 4b). It is estimated that partial recrystallization occurred for this sample, in which the recrystallized grains had small GOS values and the recovery part had high GOS values. The density of LAGBs was higher in the 10% cold rolled sample than that in the 5% cold rolled one due to the degree of deformation. Meanwhile, partial recrystallization decreased the grain size.

In the case of reductions over 15%, the samples obtained completed recrystallization during annealing. The recrystallized grain size decreased from 23.2 μm to 5.8 μm with the increasing cold rolling reductions. By comparison, a 15% cold rolling reduction is supposed to be the critical deformation for completed recrystallization of the tested C276 superalloy. The CSL fraction reached around 67% for this sample. With the further increasing rolling reductions, the CSL fraction decreased linearly.

It was found that most of the $\Sigma 3^n$ boundaries were incorporated to the HAGB networks as convoluted boundaries. Some big grain clusters can be defined, as marked in Figure 5c,d. To illustrate this more clearly, the marked areas were redrawn in Figure 9. The boundaries between grain-clusters are random HAGBs. In addition, the grains within the grain cluster have $\Sigma 3^n$ relations. Xia et al. suggested that the formation of the grain cluster is beneficial for the improvement in mechanical properties of low SFE superalloys [19,31]. The interactions between $\Sigma 3^n$ boundaries: $\Sigma 3 + \Sigma 3 \rightarrow \Sigma 9$ and $\Sigma 3 + \Sigma 9 \rightarrow \Sigma 27$, can be seen within the grain cluster.
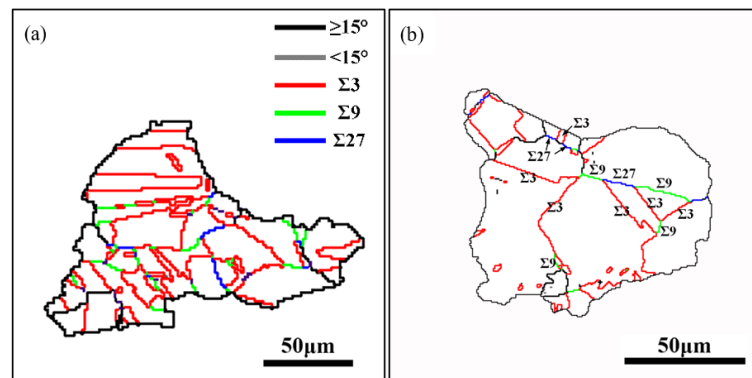
Figure 9. GBCD maps of the twin related domains. (**a**) Domain marked in rectangle in Figure 5c; (**b**) domain marked in rectangle in Figure 5d.

The parameter of $\Sigma3/(\Sigma9 + \Sigma27)$ is supposed to be related to the twining mechanism during GBE processing [23]. Randle et al. proposed two main mechanisms accounting for the proliferation of $\Sigma3^n$ boundaries, namely "$\Sigma3$ regeneration" and "new twinning" [17]. Generally, the ratio of $\Sigma3/(\Sigma9 + \Sigma27)$ can be used to determine the twin proliferation mechanism, in which a relative lower ratio implies the predominant effect of "$\Sigma3$ regeneration" while a relative higher ratio mostly corresponds to the function of "new twinning" [17,22]. As depicted in Figure 6, the ratio of $\Sigma3/(\Sigma9 + \Sigma27)$ is about 6~11, which is located in a relatively lower ratio range for superalloys as compared to previous publications [22,23]. Both the ratio of $\Sigma3/(\Sigma9 + \Sigma27)$ and the grain boundary morphology demonstrates that "$\Sigma3$ regeneration" is the governing twining mechanism for the C276 superalloy under the tested conditions.

4.2. Correlation between GBCD and IGC Resistance

Precipitates along the random grain boundaries (or HAGBs) were observed for the sensitization treated samples. It is reported that the C276 superalloy has three kinds of potential precipitates, i.e., μ, M_6C and *P* phases [32]. In a previous paper, the precipitates in the C276 superalloy's ageing, treated at 800 °C within 15 h, were confirmed to be M_6C carbides through TEM and SEM analysis [26]. The M_6C carbides were rich in Mo and W, forming a depletion zone in a width of around 2.45 μm across the grain boundaries, as defined in EPMA. Jiao et al. also calculated the Mo depletion law at grain boundaries for the C276 superalloy using John–Mel transformation kinetics and Fick diffusion law [33]. The results in this work indicated the C276 superalloy with different GBCD conditions showed obvious different precipitation tendencies. The sample with small grain size and low CSL fraction presented a more severe precipitation trend as compared to the one with a big grain size and high CSL fraction, as shown in Figure 7. The backscatter images refer that the HAGBs were the preferential precipitation sites, while hardly any precipitates were observed at the $\Sigma3^n$ boundaries. The $\Sigma3^n$ denotes the high degree of order between the lattices. These boundaries are supposed to have a high resistance to segregation, crack susceptibility, sensitization, etc. [34].

The degrees of sensitization (I_r/I_a) were different for the samples with 15% and 40% cold rolling reductions, as seen in Figure 8. It can be seen that the degree of sensitization is closely related to the precipitation behavior. With increasing the precipitates formed at grain boundaries, the IGC attacks became much more severe. The precipitation at the grain boundaries would result in a Mo/W depletion zone adjacent to the grain boundaries. These depletion zones were easily IGC attacked in the electrochemical test. Thus, the relation between the GBCD and IGC behavior for the C276 superalloy can be schematically illustrated in Figure 10. Similar Cr depletion near the grain boundaries due to the precipitation of carbides is known to deteriorate the IGC resistance of stainless steel [35].
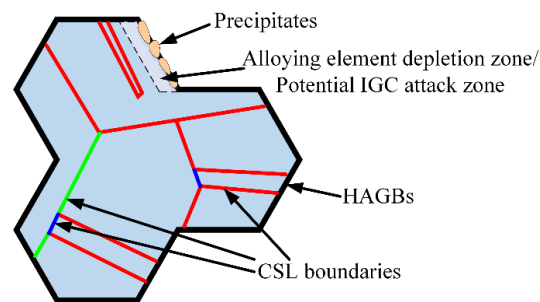
Figure 10. Schematic of the sensitized precipitation and its influence on IGC for C276 superalloy.

Based on the above analysis, it can be seen that the GBCD affected the sensitization and IGC of C276 superalloy dramatically. The GBCD can be optimized through cold rolling and annealing processes. By GBE processing, the resistances to sensitization and IGC attack can be improved. Therefore, aiming at improving the performance of C276 superalloy, it is recommended to promote the CSL fraction and grain size through GBE processing.

5. Conclusions

1. For the samples with a cold rolling reduction within 5%, recovery and limited grain growth occurred for the tested C276 superalloy during the annealing process. Partial recrystallization occurred for the sample with a cold rolling reduction of 10% during annealing, while completed recrystallization was observed for the samples with cold rolling reductions over 15%.
2. The GBCD showed as dependent on the cold rolling and annealing processes. The CSL fraction decreased after cold rolling and annealing for the samples with cold rolling reductions less than 10%. The CSL fraction reached a peak of around 67% at the 15% cold rolling and annealing at 1050 °C for 30 min, which is the critical condition for completed recrystallization.
3. A certain amount of CSL boundaries associated with the recrystallization were formed. The ratio of $\Sigma3/(\Sigma9 + \Sigma27)$ shows a relatively low value around 6~11, suggesting that "$\Sigma3$ regeneration" is the governing twining mechanism for the C276 superalloy under the tested conditions.
4. The GBCD condition affected the sensitization and IGC behaviors for C276 superalloy. The sample with a higher fraction of CSL and bigger grain size created less precipitates along grain boundaries during sensitization treatment and better IGC resistance in the DL-EPR tests.

Author Contributions: Conceptualization, C.Z., L.Z. and Z.S.; methodology and experiments, L.L., R.C. and C.Z.; writing—original draft preparation, C.Z., L.L. and R.C.; writing—review and editing, L.Z. and Z.S. All authors have read and agreed to the published version of the manuscript.

References

1. Ahmad, M.; Akhter, J.I.; Akhtar, M.; Iqbal, M.; Ahmed, E.; Choudhry, M.A. Microstructure and hardness studies of the electron beam welded zone of Hastelloy C-276. *J. Alloys Compd.* **2005**, *390*, 88–93. [CrossRef]
2. Wanderka, N.; Bakai, A.; Abromeit, C.; Isheim, D.; Seidman, D.N. Effects of 10MeV electron irradiation at high temperature of a Ni–Mo-based Hastelloy. *Ultramicroscopy* **2007**, *107*, 786–790. [CrossRef] [PubMed]
3. Guo, Y.Q.; Wu, D.J.; Ma, G.Y.; Guo, D.M. Trailing heat sink effects on residual stress and distortion of pulsed laser welded Hastelloy C-276 thin sheets. *J. Mater. Process. Technol.* **2014**, *214*, 2891–2899. [CrossRef]

4. Tan, L.; Allen, T.R.; Busby, J.T. Grain boundary engineering for structure materials of nuclear reactors. *J. Nucl. Mater.* **2013**, *441*, 661–666. [CrossRef]
5. Randle, V. Twinning-related grain boundary engineering. *Acta Mater.* **2004**, *52*, 4067–4081. [CrossRef]
6. Souaï, N.; Bozzolo, N.; Nazé, L.; Chastel, Y.; Logé, R. About the possibility of grain boundary engineering via hot-working in a nickel-base superalloy. *Scr. Mater.* **2010**, *62*, 851–854. [CrossRef]
7. Watanabe, T. Approach to grain boundary design for strong and ductile polycrystals. *Res. Mech. Int. J. Struct. Mech. Mater. Sci.* **1984**, *11*, 47–84.
8. Kuang, W.; Was, G.S.; Miller, C.; Kaufman, M.; Alam, T.; Gwalani, B.; Banerjee, R. The effect of cold rolling on grain boundary structure and stress corrosion cracking susceptibility of twins in alloy 690 in simulated PWR primary water environment. *Corros. Sci.* **2018**, *130*, 126–137. [CrossRef]
9. Deepak, K.; Mandal, S.; Athreya, C.N.; Kim, D.-I.; de Boer, B.; Subramanya Sarma, V. Implication of grain boundary engineering on high temperature hot corrosion of alloy 617. *Corros. Sci.* **2016**, *106*, 293–297.
10. Joham, R.; Sharma, N.K.; Mondal, K.; Shekhar, S. Low temperature cross-rolling to modify grain boundary character distribution and its effect on sensitization of SS304. *J. Mater. Process. Technol.* **2017**, *240*, 324–331. [CrossRef]
11. Liu, T.; Xia, S.; Bai, Q.; Zhou, B.; Zhang, L.; Lu, Y.; Shoji, T. Three-dimensional study of grain boundary engineering effects on intergranular stress corrosion cracking of 316 stainless steel in high temperature water. *J. Nucl. Mater.* **2018**, *498*, 290–299. [CrossRef]
12. Hu, C.; Xia, S.; Li, H.; Liu, T.; Zhou, B.; Chen, W.; Wang, N. Improving the intergranular corrosion resistance of 304 stainless steel by grain boundary network control. *Corros. Sci.* **2011**, *53*, 1880–1886. [CrossRef]
13. Wang, W.; Yin, F.; Guo, H.; Li, H.; Zhou, B. Effects of recovery treatment after large strain on the grain boundary character distributions of subsequently cold rolled and annealed Pb–Ca–Sn–Al alloy. *Mater. Sci. Eng. A* **2008**, *491*, 199–206. [CrossRef]
14. Yang, S.; Krupp, U.; Christ, H.-J.; Trindade, V.B. The relationship between grain boundary character and the intergranular oxide distribution in IN718 superalloy. *Adv. Eng. Mater.* **2005**, *7*, 723–726. [CrossRef]
15. Chen, A.Y.; Hu, W.F.; Wang, D.; Zhu, Y.K.; Wang, P.; Yang, J.H.; Wang, X.Y.; Gu, J.F.; Lu, J. Improving the intergranular corrosion resistance of austenitic stainless steel by high density twinned structure. *Scr. Mater.* **2017**, *130*, 264–268. [CrossRef]
16. Randle, V. Mechanism of twinning-induced grain boundary engineering in low stacking-fault energy materials. *Acta Mater.* **1999**, *47*, 4187–4196. [CrossRef]
17. Randle, V.; Owen, G. Mechanisms of grain boundary engineering. *Acta Mater.* **2006**, *54*, 1777–1783. [CrossRef]
18. Randle, V.; Hu, Y. The role of vicinal Σ3 boundaries and Σ9 boundaries in grain boundary engineering. *J. Mater. Sci.* **2005**, *40*, 3243–3246. [CrossRef]
19. Bai, Q.; Zhao, Q.; Xia, S.; Wang, B.; Zhou, B.; Su, C. Evolution of grain boundary character distributions in alloy 825 tubes during high temperature annealing: Is grain boundary engineering achieved through recrystallization or grain growth? *Mater. Charact.* **2017**, *123*, 178–188. [CrossRef]
20. Sahu, S.; Yadav, P.C.; Shekhar, S. Use of Hot Rolling for Generating Low Deviation Twins and a Disconnected Random Boundary Network in Inconel 600 Alloy. *Metall. Mater. Trans. A* **2017**, *49*, 628–643. [CrossRef]
21. Cao, Y.; Di, H.; Huang, G. On the grain boundary character distribution of Incoloy 800H during dynamic recrystallization. *J. Nucl. Mater.* **2017**, *486*, 21–25. [CrossRef]
22. Cao, Y.; Shen, X.; Di, H.; Huang, G. Texture and microstructure evolution of Incoloy 800H superalloy during hot rolling and solution treatment. *J. Alloys Compd.* **2017**, *698*, 304–316. [CrossRef]
23. Akhiani, H.; Nezakat, M.; Sanayei, M.; Szpunar, J. The effect of thermo-mechanical processing on grain boundary character distribution in Incoloy 800H/HT. *Mater. Sci. Eng. A* **2015**, *626*, 51–60. [CrossRef]
24. Akhiani, H.; Nezakat, M.; Szpunar, J.A. Evolution of deformation and annealing textures in Incoloy 800H/HT via different rolling paths and strains. *Mater. Sci. Eng. A* **2014**, *614*, 250–263. [CrossRef]
25. Jones, R.; Randle, V. Sensitisation behaviour of grain boundary engineered austenitic stainless steel. *Mater. Sci. Eng. A* **2010**, *527*, 4275–4280. [CrossRef]
26. Zhang, C.; Zhang, L.; Cui, Y.; Feng, Q.; Cheng, C. Effects of High-Temperature Aging on Precipitation and Corrosion Behavior of a Ni-Cr-Mo-Based Hastelloy C276 Superalloy. *J. Mater. Eng. Perform.* **2020**, *29*, 2026–2034. [CrossRef]
27. Momeni, M.; Moayed, M.H.; Davoodi, A. Tuning DOS measuring parameters based on double-loop EPR in H2SO4 containing KSCN by Taguchi method. *Corros. Sci.* **2010**, *52*, 2653–2660. [CrossRef]
28. Martin, U.; Ress, J.; Bosch, J.; Bastidas, D.M. Evaluation of the DOS by DL−EPR of UNSM Processed Inconel 718. *Metals* **2020**, *10*, 204. [CrossRef]
29. Zhao, H.; Zhang, Z.; Zhang, H.; Hu, J.; Li, J. Effect of aging time on intergranular corrosion behavior of a newly developed LDX 2404 lean duplex stainless steel. *J. Alloys Compd.* **2016**, *672*, 147–154. [CrossRef]
30. Martin, O.; De Tiedra, P.; San-Juan, M. Study of influence of gamma prime and eta phases on corrosion behaviour of A286 superalloy by using electrochemical potentiokinetic techniques. *Mater. Des.* **2015**, *87*, 266–271. [CrossRef]
31. Xia, S.; Zhou, B.X.; Chen, W.J.; Wang, W.G. Effects of strain and annealing processes on the distribution of Σ3 boundaries in a Ni-based superalloy. *Scr. Mater.* **2006**, *54*, 2019–2022. [CrossRef]
32. Raghavan, M.; Berkowitz, B.J.; Scanlon, J.C. Electron microscopic analysis of heterogeneous precipitates in Hastelloy C-276. *Metall. Trans. A* **1982**, *13*, 979–984. [CrossRef]

33. Jiao, S.; Zhu, G.; Dong, J.; Zhang, Q. Carbide evolution and Mo depletion law in Hastelloy C-276. *Cailiao Gongcheng/J. Mater. Eng.* **2011**, *1*, 47–52.
34. Sahu, S.; Patel, S.K.; Shekhar, S. The effect of grain boundary structure on chromium carbide precipitation in alloy 600. *Mater. Chem. Phys.* **2021**, *260*, 124145. [CrossRef]
35. Tsai, S.-P.; Makineni, S.K.; Gault, B.; Kawano-Miyata, K.; Taniyama, A.; Zaefferer, S. Precipitation formation on $\sum 5$ and $\sum 7$ grain boundaries in 316L stainless steel and their roles on intergranular corrosion. *Acta Mater.* **2021**, *210*, 116822. [CrossRef]